Design Considerations and Robustness to Parameter Uncertainty in Wire-Wrapped Cam Mechanisms

Garrison L. H. Johnston

Department of Mechanical Engineering, Vanderbilt University, Nashville, TN 37235 e-mail: Garrison.L.Johnston@vanderbilt.edu

Andrew L. Orekhov

Department of Mechanical Engineering, Vanderbilt University, Nashville, TN 37235 e-mail: Andrew.Orekhov@vanderbilt.edu

Nabil Simaan¹

Department of Mechanical Engineering, Vanderbilt University, Nashville, TN 37235 e-mail: Nabil.Simaan@vanderbilt.edu Collaborative robots must simultaneously be safe enough to operate in close proximity to human operators and powerful enough to assist users in industrial tasks such as lifting heavy equipment. The requirement for safety necessitates that collaborative robots are designed with low-powered actuators. However, some industrial tasks may require the robot to have high payload capacity and/or long reach. For collaborative robot designs to be successful, they must find ways of addressing these conflicting design requirements. One promising strategy for navigating this tradeoff is through the use of static balancing mechanisms to offset the robot's self-weight, thus enabling the selection of low-powered actuators. In this paper, we introduce a novel, two degrees-of-freedom static balancing mechanism based on spring-loaded, wire-wrapped cams. We also present an optimization-based cam design method that guarantees the cams stay convex, ensures the springs stay below their extensions limits, and minimizes sensitivity to unmodeled deviations from the nominal spring constant. Additionally, we present a model of the effect of friction between the wire and the cam. Lastly, we show experimentally that the torque generated by the cam mechanism matches the torque predicted in our modeling approach. Our results also suggest that the effects of wire-cam friction are significant for non-circular cams. [DOI: 10.1115/1.4056600]

Keywords: cable driven mechanisms, mechanism design, robot design

1 Introduction

1.1 Motivation. The United States Bureau of Labor Statistics reports that in 2015, musculoskeletal disorders (MSDs), such as pinched nerves, herniated discs, and carpal tunnel syndrome, accounted for 31% of all days-away-from-work cases reported to the agency [1]. These work-related MSDs are caused by exerting strenuous and/or repetitive forces in awkward and non-ergonomic conditions [2]. While full automation could eliminate the risk completely, the complexity of certain industrial tasks, such as equipment maintenance and repair, may necessitate a worker to be physically present at the worksite to control critical aspects of the task.

In an attempt to address this issue, there has been a recent push to develop in-situ collaborative robots (ISCRs) that can help alleviate the physiological stresses of the aforementioned tasks by exerting the potentially harmful forces while being guided by the worker using physical human-robot interaction. Because of the worker's proximity to the robot, it is absolutely imperative that the robot be endowed with both active and passive measures of safety. Active safety measures, such as collision detection and avoidance algorithms, are safeguards against injury coded into the robot's control system. Passive safety measures, on the other hand, are features built into the robot's mechanical design that minimize the likelihood of trauma in the case of a collision between the robot and the worker. Designing a robot with as low-powered actuators as possible can effectively increase the passive safety of the device, especially in the case of catastrophic control system failure. By removing the need for the actuators to lift the robot's self-weight,

static balancing mechanisms are a promising way of lowering actuator torque requirements and thereby achieving higher levels of passive safety [3].

1.2 Relevant Works and Summary of Limitations. Static balancing mechanisms are typically realized using either counterbalancing masses (e.g., Refs. [4–6]), springs, or a combination of both [4,7]. Spring-based static balancing mechanisms offer the advantage of lower overall mass and inertia compared to counterbalancing, making them an attractive option for safety, but come at the cost of higher design and modeling complexity. Spring-based static balancing methods have mostly fallen into three categories: (1) spring-loaded linkages [8–14], (2) cams with spring-loaded followers [15–19], and (3) wire-wrapped cams [20–31]. Additionally, many simple balancing mechanisms are presented in Ref. [32].

It is possible to achieve exact static balancing of planar linkages by using zero-length springs and parallelogram linkages [11,33,34]. While these design solutions may yield acceptable embodiments for certain applications, it may be preferable to consider designs that do not increase the footprint of the manipulator's linkages because of the restricted nature of some applications. A potential solution for this could be the more compact designs presented in Refs. [35,36]. However, these designs are very complex and add many components such as springs, bevel gears, linear bearings, and linear slides into the linkages of the robot. This increases the mass and inertia of the robot, thus reducing its safety. Therefore, there is interest in keeping as many balancing components as possible at the base of the robot.

This paper will focus on wire-wrapped cam methods. These mechanisms are typically realized with a wire that is fixed to the cam on one end, goes over an idler pulley, and is attached to a linear spring at the other end. When the cam rotates, it wraps the wire over the cam, inducing a torque on the cam from the resulting spring deflection. From a given spring constant, the cam profile can

¹Corresponding author.

Contributed by Mechanisms and Robotics Committee of ASME for publication in the JOURNAL OF MECHANISMS AND ROBOTICS. Manuscript received June 24, 2022; final manuscript received December 21, 2022; published online March 3, 2023. Assoc. Editor: Kwok Wai Samuel Au.

be specially designed to match a desired torque profile as a function of cam angle. Previous works in these areas have used either closedform equations (e.g., Ref. [23]) or graphical synthesis (e.g., Ref. [28]) to determine the profile of the cam. These methods can provide a cam profile that will generate the desired torque profile exactly. However, they suffer from multiple drawbacks. For certain desired torque profiles, (1) the methods can return nonconvex cams (which are needed for continued tangency between the wrapped wire and the cam), (2) there is no explicit guarantee the spring stay below the maximum allowable deflection and in many cases necessitate unrealistically large spring deflections, and (3) there is no consideration of how uncertainty in the spring stiffness may affect the balancing performance. Additionally, previous works have treated the torque on the cam as resulting from a point force applied at the wire-cam tangency point, ignoring the distributed friction, and pressure between the rest of the wire and the cam.

While it may be feasible to search for a set of input parameters that address the non-convexity problem of the closed-form solution, we believe this may not always be a feasible approach. The location and size of the idler are subject to space constraints. Similarly, the cam size is also governed by geometric constraints within a realistic design. The spring parameters that would satisfy cam convexity may also not be feasible when realistic spring design considerations are applied. Finally, this process of sampling the design space is essentially a time-consuming, ad-hoc design optimization process. In this paper, we offer an alternative approach that allows automatic consideration of geometric constraints, robustness to variation in spring parameters, and cam convexity. As such, our approach offers a design that considers realistic constraints while offering the best feasible approximation for the static balancing problem.

Design optimization for static balancing has been used in the past to determine which static robot configuration to perfectly balance to achieve the best balancing across its workspace [37] and to select torsional springs to balance a medical robot [38]. It has also been used to determine the Fourier coefficients of the cam dynamic equations [39] and to optimize mechanism parameters for multi-degrees-of-freedom (DOF) robots [40]. To the best of our knowledge, design optimization has not been used to address the concerns with wire-wrapped cams listed in the previous paragraph.

1.3 Contribution and Paper Organization. The contribution of this paper relative to previous works is a cam design procedure that uses optimization to select modal coefficients for the cam shape and spring pre-extensions that minimize the difference between the actual cam torque and the desired cam torque. It also minimizes the sensitivity of the output torque to unanticipated changes in spring constant. The optimization problem is constrained to guarantee cam convexity and ensures the cam will not violate the maximum allowable spring deflections. As an additional contribution of this work, we model the effect of friction between the cam and the wire. This optimization routine is applied to a novel two DOF cam design. This two DOF system can be used for systems when the desired torque on one or both cams is a function of both cam angles. The major drawback of our method is that the torque on the cams is not guaranteed to exactly match the desired torque. However, for robotic applications, it is much more desirable to have a physically build-able cam system that approximately balances the static torques than a cam design that theoretically, exactly balances the static torques but violates the maximum allowable spring extensions and is not convex (i.e., does not work in practice).

This paper is organized as follows. In Sec. 2, we present the design of a novel one DOF cam system and solve for the wire tangency point. In Sec. 3, we solve for the spring extensions for the one DOF cam design and extend the equations for a two DOF cam design. Later, in Sec. 4, we calculate the torque on the one DOF cam system with and without ignoring frictional effects. In Sec. 5, we extend the equations for the two DOF cam design. Then in Sec. 6, we describe the modal basis chosen for the cam design and derive the conditions on the cam modal basis required for

cam convexity. In Sec. 7, we derive a first-order approximation of the sensitivity of the cam torque to unmodeled changes in spring torque. The optimization problem used to design the cams is formulated in Sec. 8. In Sec. 10, we present the results of two simulation case studies, and in Sec. 11 our model for the torque on the cams is experimentally validated. Lastly, the results are discussed in Sec. 12 and conclusions are drawn in Sec. 13.

2 The Tangency Points in a Wire-Cam Mechanism

The calculation of spring extensions in wire-cam mechanisms requires knowledge of the tangency point between the idler and the cam. In this section, we present a numerical solution to finding the tangency point for a general wire-cam design. Specifically, we refer the reader to Fig. 1, where a follower idler is pressed horizontally against the cam using one spring and the wire rope is tensioned using another spring. Figure 1(a) shows the system with initial spring preload and zero cam rotation. Figure 1(b) shows the same system for a cam rotation $\theta > 0$.

The spring extensions x_1 and x_2 shown in Fig. 1(b) are functions of the angles α and γ . These two angles characterize the location of the tangency point **p** on the cam and idler, respectively. To solve for these angles, we use the fact that the cam and idler are tangent to one another at **p**. To do this, we will calculate the unit vectors that are tangent to the cam $\hat{\mathbf{t}}(\alpha)$ and idler $\hat{\mathbf{t}}(\gamma)$ and set them equal.

The local tangents to the cam and idler, $\mathbf{t}(\alpha)$ and $\mathbf{t}(\gamma)$ are shown in Fig. 1. These vectors are defined as

$$\mathbf{t}(\alpha) = \frac{d}{d\alpha} \mathbf{r}_{p/o}, \quad \mathbf{t}(\gamma) = \frac{d}{d\gamma} \mathbf{r}_{p/q}$$
 (1)

where the position vectors $\mathbf{r}_{p/o}$ and $\mathbf{r}_{p/q}$ are given by²

$$\mathbf{r}_{p/o} = \rho(\alpha) \begin{bmatrix} \cos(\alpha - \theta) \\ \sin(\alpha - \theta) \\ 0 \end{bmatrix}, \quad \mathbf{r}_{p/q} = r \begin{bmatrix} \cos(\gamma) \\ \sin(\gamma) \\ 0 \end{bmatrix}$$
 (2)

The explicit expressions for these tangent vectors are

$$\mathbf{t}(\alpha) = \rho'(\alpha) \begin{bmatrix} \cos{(\alpha - \theta)} \\ \sin{(\alpha - \theta)} \\ 0 \end{bmatrix} + \rho(\alpha) \begin{bmatrix} -\sin{(\alpha - \theta)} \\ \cos{(\alpha - \theta)} \\ 0 \end{bmatrix}$$
(3)

$$\mathbf{t}(\gamma) = r[-\sin(\gamma), \cos(\gamma), 0]^{\mathrm{T}}$$
(4)

Normalizing these vectors using $\|\mathbf{t}(\alpha)\| = \sqrt{\rho(\alpha)^2 + \rho'(\alpha)^2}$ and $\|\mathbf{t}(\gamma)\| = r$ gives the local tangent unit vectors

$$\hat{\mathbf{t}}(\alpha) = \frac{\mathbf{t}(\alpha)}{\sqrt{\rho(\alpha)^2 + \rho'(\alpha)^2}} \quad \hat{\mathbf{t}}(\gamma) = \frac{\mathbf{t}(\gamma)}{r}$$
 (5)

The local tangency constraint between the idler and cam is

$$\hat{\mathbf{t}}(\alpha) = -\hat{\mathbf{t}}(\gamma) \tag{6}$$

The above constraint could be solved numerically, but can return more than one answer if α and γ are not related through an added constraint. We choose the constraint that the y coordinate of $\mathbf{r}_{p/o}$ is equal to sum of the y coordinates of $\mathbf{r}_{q/o}$ and $\mathbf{r}_{p/q}$. For example, if $\mathbf{r}_{q/o}^{\mathbf{T}}\hat{\mathbf{y}}_0 = a_0$ (i.e., the vertical offset of the idler in Fig. 1), then

$$\rho(\alpha)\sin(\alpha - \theta) = r\sin(\gamma) + a_0 \tag{7}$$

Combining Eq. (6) with Eq. (7) allows us to formulate the following optimization problem

$$\min_{\alpha, \gamma} \quad \|\hat{\mathbf{t}}(\alpha) + \hat{\mathbf{t}}(\gamma)\|^2 + \left(\rho(\alpha)\sin(\alpha - \theta) - r\sin(\gamma) - a_0\right)^2 \quad (8)$$

²We use $\mathbf{r}_{x/y} \triangleq \mathbf{x} - \mathbf{y}$ where $\mathbf{x} \in \mathbb{R}^3$ and $\mathbf{y} \in \mathbb{R}^3$ are points.

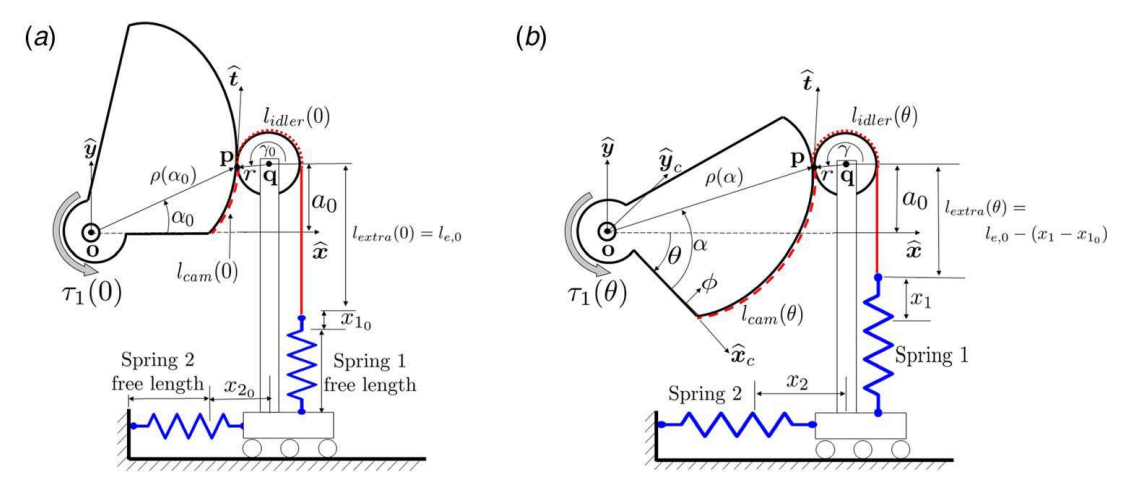


Fig. 1 Cam design concept for a 1DOF system: (a) $\theta = 0$ and (b) $\theta > 0$

For any cam angle θ , the Levenberg–Marquardt algorithm [41] can be used to solve for α and γ (e.g., using MATLAB's *lsqnonlin* function).

3 Spring Extensions for Wire-Cam Mechanisms

Next, we will determine the spring deflections for design variants with one and two DOF.

3.1 One Degree-of-Freedom Wire-Wrapped Cams. Referring to Fig. 1, the deflection in spring 1 can be solved using the assumption that the length l of the wire remains constant. This wire length is shown in Fig. 1 as the sum of three portions shown using dashed line l_{cam} , dotted line l_{idler} , and solid line l_{extra} .

$$l = l_{cam} + l_{idler} + l_{extra} (9)$$

 l_{cam} can be found using the line integral along the cam from 0 to α . The profile of the cam is expressed using the polar function $\rho(\phi)$ where ϕ parameterizes the angle swept along the cam. This line integral can be written as

$$l_{cam} = \int_0^\alpha \sqrt{\rho(\phi)^2 + \rho'(\phi)^2} \, d\phi \tag{10}$$

Next, l_{idler} can be expressed as

$$l_{idler} = r\gamma \tag{11}$$

where r is the radius of the idler and γ is the angle between the horizontal and the idler tangency point as shown in Fig. 1. Now, l_{extra} can be found using

$$l_{extra} = l_{e,0} - (x_1 - x_{1_0}) \tag{12}$$

In this equation, $l_{e,0}$ is the length of wire between spring 1 when $\theta = 0$, x_1 is the total extension of spring 1, and x_{1_0} is the extension of spring 1 when $\theta = 0$ (i.e., the pre-extension of spring 1). Because the wire is inextensible, the change in string length between when $\theta > 0$ and $\theta = 0$ (i.e., $\Delta l \triangleq l(\theta) - l(0)$) must be zero

$$\Delta l = \Delta l_{cam}(\theta) + \Delta l_{idler}(\theta) + \Delta l_{extra}(\theta) = 0$$
 (13)

where the length change terms in Eq. (13) are measured with respect to the respective lengths when $\theta = 0$.

Plugging Eqs. (10)–(12) into Eq. (13) and solving for x_1 gives

$$x_1 = \int_{\alpha_0}^{\alpha} \sqrt{\rho(\phi)^2 + \rho'(\phi)^2} \, d\phi + r(\gamma - \gamma_0) + x_{1_0}$$
 (14)

The vector $\mathbf{r}_{a/o} \triangleq \mathbf{q} - \mathbf{o}$ is calculated as

$$\mathbf{r}_{q/o} = \begin{bmatrix} \rho(\alpha)\cos(\alpha - \theta) - r\cos(\gamma) \\ a_0 \\ 0 \end{bmatrix}$$
 (15)

The total extension of spring 2 can be found using its preextension x_{20} and the change in the x component of $\mathbf{r}_{a/o}$

$$x_2 = \rho(\alpha)\cos(\alpha - \theta) - r\cos(\gamma) - (\rho(\alpha_0)\cos(\alpha_0) - r\cos(\gamma_0)) + x_{2_0}$$
(16)

3.2 Two Degrees-of-Freedom Wire-Wrapped Cams. A two DOF design variant is shown in Fig. 2. This system is designed so that the torque on the cams are functions of both cam angles (i.e., $\tau_1(\theta_1, \theta_2)$ and $\tau_1(\theta_1, \theta_2)$). A planar RR (R refers to a revolute joint) manipulator arm is a potential application of this design variant. This system contains two cams with very similar structure to the one DOF cam system shown in Fig. 1. However, instead of being connected to ground, spring 2 connects the prismatic platforms for both cams. This means that changing θ_1 affects the torque on cam 2 and vice versa. In this section, we again assume infinite friction between the cam and wire and assume that the springs are linear functions of displacement.

Because the angles α_1 and γ_1 are independent of θ_2 and α_2 and γ_2 are independent of θ_1 , the equations in Sec. 2 can be directly applied to solve for the tangency angles of each cam.

Next, we will derive the spring displacements x_1 , x_2 , and x_3 . Because the displacement of springs 1 and 3 does not depend on the angle of the cam they are not wrapped around, Eq. (14) can be used to solve for the spring displacements x_1 and x_3 as shown in Fig. 2. Because the displacement of spring 2 depends on both θ_1 and θ_2 , we must apply Eq. (16) to solve for the displacement of spring 2 while taking into account the individual contributions

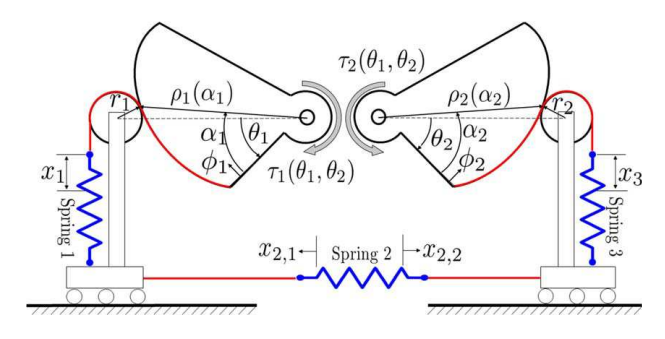


Fig. 2 Cam design concept for a two DOF system

of each cam. To designate the contribution of cam i to the extension of spring 2 we use the notation $x_{2,i}$, i = 1, 2. Referring to Fig. 2, we can write the extension of the second spring

$$x_2 = x_{20} + x_{2,1} + x_{2,2} (17)$$

where x_{2_0} is the initial spring extension and the individual cam contributions to the spring extension are given by

$$x_{2,i} = \rho_i(\alpha_i)\cos(\alpha_i - \theta_i) - r_i\cos(\gamma_i) - (\rho_i(\alpha_{i_0})\cos(\alpha_{i_0}) - r_i\cos(\gamma_{i_0})), \quad i = 1, 2$$
(18)

where the subscript i indicates the cam number. Having expressed the spring extensions due to cam rotations, we next compute the resulting balancing torques. In the beginning of Sec. 4, we consider a model using a practice prevalent in the literature which assumes infinite friction between the cam and wire. In Sec. 4.1, we relax the assumption of infinite friction and present a model that accounts for a finite friction coupling between the cam and wire.

4 One Degree-of-Freedom Wire-Wrapped Cam Torque

Substituting the solution of Eq. (8) for α and γ in Eqs. (14) and (16) provides the spring extensions x_1 and x_2 . Assuming infinite friction coupling and referring to Fig. 1, the force \mathbf{f}_1 applied by the wire rope on the cam is concentrated at the tangency point \mathbf{p} and pointing tangential to the cam

$$\mathbf{f}_1 = k_1 x_1 \hat{\mathbf{t}} \tag{19}$$

In this equation, k_1 is the stiffness of spring 1 and $\hat{\mathbf{t}} = \hat{\mathbf{t}}(\alpha) = -\hat{\mathbf{t}}(\gamma)$ is a unit vector tangent to the idler/cam contact given by Eq. (5). The moment of spring 1 on the cam is the cross-product of $\mathbf{r}_{p/o}$ and \mathbf{f}_1 . Similarly, the force applied by spring 2 on the cam is

$$\mathbf{f}_2 = k_2 x_2 \hat{\mathbf{n}} \tag{20}$$

where k_2 is the stiffness of spring 2 and $\hat{\mathbf{n}} = (d/d\alpha)\hat{\mathbf{t}}(\alpha) = -(d/d\gamma)\hat{\mathbf{t}}(\gamma)$ is the unit vector normal to the idler/cam contact. The moment of spring 1 on the cam is the cross-product of $\mathbf{r}_{p/o}$ and \mathbf{f}_2 .

The scalar moment acting on the cam is given by the spring force moments about point \mathbf{o} , therefore

$$\tau_1 = (\underbrace{\mathbf{r}_{p/o} \times \mathbf{f}_1}_{\tau_{1,1}} + \underbrace{\mathbf{r}_{p/o} \times \mathbf{f}_2}_{\tau_{1,2}})^{\mathrm{T}} \hat{\mathbf{z}}$$
(21)

where the single subscript in τ_1 designates the cam number. It is included to maintain consistency with the notation for the two DOF case. Also, in $\tau_{1,1}$ and $\tau_{1,2}$ the first subscript refers to the cam number and the second subscript refers to the spring number.

4.1 Wire-Wrapped Cam Torque With Finite Friction Coupling. In this section, we explore the effect of finite capstan/ wire-rope friction on the resulting torque on the cam. We model the forces at a quasi-static equilibrium where we assume θ is fixed.

4.1.1 Wire Model. We will assume that the wire is inextensible and can only support tension forces (i.e., it cannot support transverse shear forces and bending moments). The tendon curve is assumed to match the planar cam shape parameterized by angle ϕ , as shown in Fig. 1(b).

Following Ref. [42], we define the wire *internal force* $\psi(\phi) \in \mathbb{R}^3$ as the force applied by the material at $\phi + \delta \phi$ on the material at ϕ . To be bent into the cam curve, the wire must have an external force or moment distribution applied to it. Referring to Fig. 3, we use \mathbf{f}_c to designate the distributed normal/contact force between the wire and the cam and \mathbf{f}_f as the distributed friction force between the

wire and the cam. The force balance for a section $[a, \phi]$ is given by

$$\psi(\phi) - \psi(a) + \int_{a}^{\phi} \mathbf{f}(\sigma) d\sigma = 0$$
 (22)

where \mathbf{f} is the resultant of the contact and friction force on the wire (per unit of wrapping angle ϕ)

$$\mathbf{f} = \mathbf{f}_f + \mathbf{f}_c \tag{23}$$

We then take a derivative of this with respect to ϕ

$$\psi'(\phi) + \mathbf{f}(\phi) = 0 \tag{24}$$

where (') denotes a derivative with respect to ϕ .

Assuming the tendon is always in contact with the cam, and since the internal force is always tangent to the wire path (since the wire cannot support transverse shear and moment loads), we can write the internal force in the wire

$$\psi(\phi) = \eta(\phi) \frac{\mathbf{r}'(\phi)}{\|\mathbf{r}'(\phi)\|} \tag{25}$$

where $\mathbf{r}'(\phi)/\|\mathbf{r}'(\phi)\|$ designates the local tangent, which can be found using a similar derivation of $\mathbf{t}(\alpha)$ in Eq. (3), but for $\alpha - \theta = \phi$. Also, $\eta(\phi) > 0$ designates the wire tension and $\mathbf{r}(\phi)$ denotes the polar vector in a cam-attached frame.

$$\mathbf{r}(\phi) = \rho(\phi)[\cos(\phi), \sin(\phi), 0]^{\mathrm{T}}$$
 (26)

4.1.2 Capstan Equation. We next derive the tension distribution $\eta(\phi)$ following the approach in Ref. [43]. Referring to the wire rope segment shown in Fig. 4, we define the distributed normal force dN over a wire segment given by $d\phi$ and the tension force magnitudes given by $\eta(\phi)$ and $\eta(\phi) + d\eta$. Writing the force balance on this infinitesimal wire segment yields

$$dN = (\eta + d\eta) \sin \frac{d\phi}{2} + \eta \sin \frac{d\phi}{2}$$
 (27a)

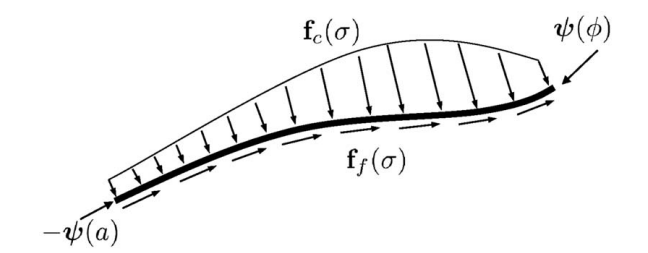


Fig. 3 Free body diagram of the wire with distributed loads and

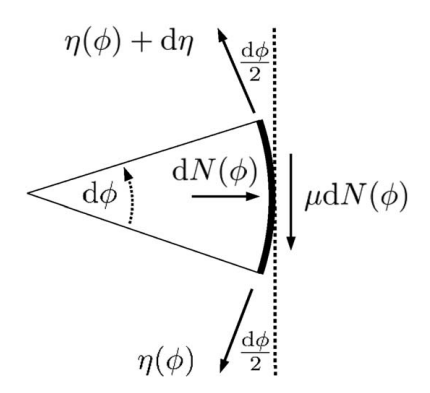


Fig. 4 Differential forces due to friction between the cam and the wire

$$(\eta + d\eta)\cos\frac{d\phi}{2} = \eta\cos\frac{d\phi}{2} + \mu dN$$
 (27b)

Applying small angle approximations $\sin \phi \approx \phi$, $\cos \phi \approx 1$ and neglecting the product of two small differentials, we get

$$dN = (\eta + d\eta) \frac{d\phi}{2} + \eta \frac{d\phi}{2} \approx \eta \, d\phi$$
 (28a)

$$\mu \, \mathrm{d}N = \mathrm{d}\eta \tag{28b}$$

Substituting Eq. (28a) into Eq. (28b), separating variables, and integrating from the initial angular coordinate ϕ up to the roller/cam tangency point (designated by angular coordinate α) results in

$$\int_{\phi}^{\alpha} \mu \, \mathrm{d}\phi = \int_{\eta(\phi)}^{\eta(\alpha)} \frac{1}{\eta} \, \mathrm{d}\eta \tag{29}$$

Writing the above integrals and taking the exponent, gives

$$e^{\mu(\alpha-\phi)} = \frac{\eta(\alpha)}{\eta(\phi)} \tag{30}$$

Solving for the wire tension $\eta(\phi)$ at any location ϕ gives

$$\eta(\phi) = \eta(\alpha)e^{\mu(\phi - \alpha)} \quad \phi \in [0, \, \alpha] \tag{31}$$

Next, we will use this result to compute the distributed force in the wire and the resulting torque on the cam.

4.1.3 Distributed Wire Force and Cam Torque. The wire force vector was given by Eq. (25). Substituting Eq. (31) in Eq. (25) gives

$$\psi(\phi) = \eta(\alpha)e^{\mu(\phi-\alpha)} \frac{\mathbf{r}'(\phi)}{\|\mathbf{r}'(\phi)\|}$$
(32)

Differentiating the above equation with respect to ϕ gives

$$\boldsymbol{\psi}'(\phi) = \frac{\eta(\alpha)e^{\mu(\phi-\alpha)}}{\|\mathbf{r}'\|} \left(\mu\mathbf{r}' + \mathbf{r}'' - \mathbf{r}'(\mathbf{r}'^{\mathrm{T}}\mathbf{r}')^{3}(\mathbf{r}''^{\mathrm{T}}\mathbf{r}')\right)$$
(33)

Using the above result in Eq. (24), we obtain the resultant distributed force on the wire

$$\mathbf{f}(\phi) = -\frac{\eta(\alpha)e^{\mu(\phi - \alpha)}}{\|\mathbf{r}'\|} \left(\mu\mathbf{r}' + \mathbf{r}'' - \mathbf{r}'(\mathbf{r}'^{\mathrm{T}}\mathbf{r}')^{3}(\mathbf{r}''^{\mathrm{T}}\mathbf{r}')\right)$$
(34)

The torque applied by the wire on the cam is given by the moment arm of the force ψ at the wire-anchor-point $\phi = 0$ and the moment of the distributed force $\mathbf{f}(\phi)$

$$\tau_{1,1} = \mathbf{r}(0) \times \boldsymbol{\psi}(0) + \int_{0}^{\alpha} \mathbf{r}(\sigma) \times -\mathbf{f}(\sigma) \, d\sigma$$
 (35)

This is an alternate formulation for $\tau_{1,1}$ given in Eq. (21) that now removes the assumption of infinite friction.

5 Two Degrees-of-Freedom Wire-Wrapped Cams

Regardless of the type of friction coupling between the cam and the wire rope, the results for the two DOF case are simply a superposition of the reactions applied by each spring on each cam. Referring to Fig. 2, we note that cam 1 is subject to torque contributions from spring 1 and spring 2. Similarly, cam 2 is subject to torque contribution due to reactions from spring 2 and spring 3. Adopting the notation $\tau_{i,j}$ to designate the torque contribution of spring j on cam i, we can write

$$\boldsymbol{\tau}_i = \left(\boldsymbol{\tau}_{i,i} + \boldsymbol{\tau}_{i,i+1}\right)^{\mathrm{T}} \hat{\mathbf{z}} \quad i = 1, 2$$
 (36)

For the two DOF cam system shown in Fig. 2, the torque on cam 1 and cam 2, τ_1 and τ_2 , can be found by applying the equations from Sec. 4 using the spring displacements from Sec. 3.2. $\tau_{2,3}$ should be calculated using Eqs. (21) or (35).

We will next present considerations for cam convexity, which will feed into the cam optimization process.

6 Modal Cam Shape and Condition for Convexity

In this work, we represent the profile of the cam profile using a polar representation

$$x(\phi) = \rho(\phi)\cos(\phi) \quad y(\phi) = \rho(\phi)\sin(\phi) \tag{37}$$

where ρ and ϕ are the radial and polar coordinates. The radial coordinate $\rho(\phi)$ can be expressed via a modal representation

$$\rho(\phi) = \boldsymbol{\beta}^{\mathrm{T}} \begin{bmatrix} 1, & \phi, & \phi^2, & \dots, & \phi^{n-1}, & \phi^n \end{bmatrix}^{\mathrm{T}}$$
 (38)

where $\beta \in \mathbb{R}^{n+1}$ is a vector of polynomial coefficients.

In making the above choice of using a polynomial basis, we implicitly limit ourselves to cam representations with orders below n=7 since polynomial bases are known to suffer from poor numerical conditioning for large powers (n>7) [44].

In order for the wire to maintain contact with the cam, the cam should be convex at all points along its surface. As shown in Ref. [45], a curve $f:(x(\phi), y(\phi)) \to \mathbb{R}^2$ is convex if

$$x'(\phi)y''(\phi) - y'(\phi)x''(\phi) > 0, \quad \forall \phi$$
 (39)

where $(\cdot)'$ and $(\cdot)''$ designate first and second derivatives with respect to ϕ . Using Eq. (37) in Eq. (39) yields the constraint for ensuring cam convexity

$$\rho(\phi)^{2} + 2\rho'(\phi)^{2} - \rho(\phi)\rho''(\phi) > 0 \tag{40}$$

7 Sensitivity to Changes in Spring Constant

If a cam design has one spring with constant k, the cam torque deviation $\Delta \tau$ for a fixed cam angle that ensues due to spring constant deviation Δk can be found using a first-order approximation [46]

$$\Delta \tau = \frac{\partial \tau}{\partial k} \Delta k \tag{41}$$

For the one DOF cam, to minimize the effect of deviations in spring constant, the design parameters (the cam modal coefficients β and the spring pre-extensions \mathbf{x}_0) are selected to minimize the following weighted sum

$$\min_{\boldsymbol{\beta}, \mathbf{x}_0} \left(\sum_{i=1}^2 w_{1,i} \int_{\theta_{min}}^{\theta_{max}} \left| \frac{\partial \tau_1}{\partial k_i} \right| d\theta \right) \tag{42}$$

where τ_1 is given by Eq. (21). The scalar weights $w_{1,1}$ and $w_{1,2}$ represent the relative importance of minimizing the effect of unmodeled deviations in the stiffness of springs 1 and 2, respectively. For example, larger weights can be set for springs with larger uncertainty in their spring constant.

For the infinite friction case, we note that $\partial \tau_{1,1}/\partial k_2 = \partial \tau_{1,2}/\partial k_1 = \mathbf{0}$ and use the commutativity of the dot product in Eq. (21), to obtain

$$\frac{\partial \tau_1}{\partial k_1} = \hat{\mathbf{z}}^{\mathrm{T}} \left(\mathbf{r}_{p/o} \times x_1 \hat{\mathbf{t}} \right), \quad \frac{\partial \tau_1}{\partial k_2} = \hat{\mathbf{z}}^{\mathrm{T}} \left(\mathbf{r}_{p/o} \times x_2 \hat{\mathbf{n}} \right)$$
(43)

For the finite friction case, the partial of τ_1 with respect to k_2 remains the same as in Eq. (43). However, the partial of τ_1 with respect to k_1 needs to be updated with the equations in Sec. 4.1. Given that the wire tension at the contact point is $\eta(\alpha) = k_1 x_1$, this can be found by taking the partial of Eq. (35)

$$\frac{\partial}{\partial k_{1}} \tau_{1} = \hat{\mathbf{z}}^{T} \left(\mathbf{r}(0) \times x_{1} e^{-\mu \alpha} \frac{\mathbf{r}'(0)}{\|\mathbf{r}'(0)\|} + \int_{0}^{\alpha} \mathbf{r}(\sigma) \times \frac{x_{1} e^{\mu(\sigma - \alpha)}}{\|\mathbf{r}'\|} \left(\mu \mathbf{r}' + \mathbf{r}'' - \mathbf{r}' (\mathbf{r}'^{T} \mathbf{r}')^{3} (\mathbf{r}''^{T} \mathbf{r}') \right) d\sigma \right) \tag{44}$$

The two DOF design in Fig. 2 has three springs and two cams, the objective function is therefore modified as

$$\min_{\boldsymbol{\theta}_{1}, \boldsymbol{\beta}_{2}, \mathbf{x}_{0}} \left(\sum_{i=1}^{3} w_{1,i} \int_{\theta_{2,min}}^{\theta_{2,max}} \int_{\theta_{1,min}}^{\theta_{1,max}} \left| \frac{\partial \tau_{1}}{\partial k_{i}} \right| d\theta_{1} d\theta_{2} + \sum_{i=1}^{3} w_{2,i} \int_{\theta_{2,min}}^{\theta_{2,max}} \int_{\theta_{1,min}}^{\theta_{1,max}} \left| \frac{\partial \tau_{2}}{\partial k_{i}} \right| d\theta_{1} d\theta_{2} \right)$$
(45)

In this equation, τ_i , i = 1, 2, are given by Eq. (36) and $w_{1,i}$ $w_{2,i}$ are scalar weights representing the relative importance of minimizing the effect of uncertainty in spring i on torques for cams 1 and 2.

8 Optimal Wire-Cam Mechanism Design

8.1 One Degree-of-Freedom Cam System. Now that we can calculate the torque on the cam from Sec. 4 and the sensitivity of the torque to unmodeled changes in the spring constant from Sec. 7, we can formulate the optimization problem used to design the cam system. The optimization variables used for this problem are the cam polynomial coefficients $\boldsymbol{\beta}$ and the spring pre-extensions $\mathbf{x}_0 = \begin{bmatrix} x_{1_0} & x_{2_0} \end{bmatrix}$. The following parameters are taken to be constants: the idler radius r, the spring constants k_i , i=1, 2, the maximum spring deflections $x_{i,max}$, and the wire-cam coefficient of friction μ . The desired cam torque $\tau_d(\theta)$, which is the torque needed to statically balance the joint, is also taken as an input. The condition for convexity from Sec. 6 and practical limits on the cam geometry and spring deflections are taken as constraints

$$\begin{aligned} \min_{\boldsymbol{\theta},\mathbf{x}_{0}} \quad w_{1} \int_{\theta_{min}}^{\theta_{max}} \left(\tau_{d,1}(\boldsymbol{\theta}) - \tau_{1}(\boldsymbol{\theta})\right)^{2} d\boldsymbol{\theta} + \sum_{i=1}^{2} w_{i+1} \int_{\theta_{min}}^{\theta_{max}} \left| \frac{\partial \tau_{1}(\boldsymbol{\theta})}{\partial k_{i}} \right| d\boldsymbol{\theta} \\ s.t. \qquad \qquad \rho^{2} + 2\rho'^{2} - \rho\rho'' > 0 \qquad \qquad (46) \\ \rho_{min} < \rho < \rho_{max} \\ 0 \le x_{i} < x_{i,max}, \quad i = 1, 2 \\ \mathbf{0} \le \mathbf{x}_{0} \end{aligned}$$

where w_1 , w_2 , and w_3 are scalar weights which represent the relative importance of the terms.

8.2 Two Degrees-of-Freedom Cam System. For the two DOF system, the desired torque on the cams may be functions of both cam angles: $\tau_{d,1}(\theta_1,\theta_2)$ and $\tau_{d,2}(\theta_1,\theta_2)$. The cam 1 polynomial coefficients $\boldsymbol{\beta}_1$, cam 2 polynomial coefficients $\boldsymbol{\beta}_2$ and spring preextensions $\mathbf{x}_0 = \begin{bmatrix} x_{1_0} & x_{2_0} & x_{3_0} \end{bmatrix}$ are the optimization variables. We also assume that the desired cam torques $\tau_{d,1}(\theta_1,\theta_2)$ and $\tau_{d,2}(\theta_1,\theta_2)$ are specified by the design task (i.e., the static balancing torques). In the equation below, the arguments from $\tau_t(\theta_1,\theta_2)$, t=1, 2 and $\tau_{d,t}(\theta_1,\theta_2)$ t=1, 2 are dropped for notational brevity.

$$\min_{\theta_{1},\theta_{2},\mathbf{x}_{0}} \qquad \int_{\theta_{min,2}}^{\theta_{max,2}} \int_{\theta_{min,1}}^{\theta_{max,1}} \sum_{j=1}^{2} w_{j} (\tau_{d,j} - \tau_{j})^{2} d\theta_{1} d\theta_{2}
+ \sum_{i=1}^{3} w_{i+2} \int_{\theta_{min,2}}^{\theta_{max,2}} \int_{\theta_{min,1}}^{\theta_{max,1}} \left| \frac{\partial \tau_{1}}{\partial k_{i}} \right| d\theta_{1} d\theta_{2}
+ \sum_{i=1}^{3} w_{i+5} \int_{\theta_{min,2}}^{\theta_{max,2}} \int_{\theta_{min,1}}^{\theta_{max,1}} \left| \frac{\partial \tau_{2}}{\partial k_{i}} \right| d\theta_{1} d\theta_{2}$$

$$s.t. \qquad \qquad \rho_{i}^{2} + 2\rho_{i}^{2} - \rho_{i}\rho_{i}^{"} > 0, \quad i = 1, 2$$

$$\qquad \qquad \rho_{min} < \rho_{i} < \rho_{i,max}, \quad i = 1, 2$$

$$\qquad \qquad 0 \le x_{0}$$

$$\qquad \qquad 0 \le x_{0}$$

where w_1 through w_8 are scalar weights which represent the relative importance of the terms. For example, a spring with a loose manufacturer-specified stiffness tolerance would require a higher weight to reduce the effect of this variability on the cam torque error.

9 Wire-Cam Coefficient of Friction Characterization

Because the static coefficient of friction is used as an input into Eq. (47), we must characterize the static coefficient of friction between the cam and the wire before we can use Eq. (47) to solve for the cam shape. In this work, we 3D printed the cams using FormlabsTM Grey Pro resin and chose the wire to be a stainless steel, 7×49 construction, 0.08 in. diameter wire rope. To test the static coefficient of friction between these materials, we printed a cylindrical portion of the cam material (② in Fig. 5) and draped the wire over the cylinder such that it was wrapped 180° along the cylinder's circumference as shown in Fig. 5. A small force f_0 was added to one end of the wire and then a force was added to the other end of the wire until static friction was broken and the wire slipped. The slippage force f was recorded and the coefficient of friction was calculated using the capstan equation

$$\mu = \frac{1}{\pi} \ln \left(\frac{f}{f_0} \right) \tag{48}$$

This experiment was repeated ten times. The mean coefficient of friction was found to be 0.3273 with a standard deviation of 0.0274.

10 Simulation Case Studies

10.1 Comparison to Closed-Form Solution. To demonstrate the benefit of our approach relative to the closed-form solution, we offer here an example of a single-DOF cam design for satisfying the desired torque function $\tau_d = 0.08\theta^2$. Figure 6 shows a comparison of our method to the method of Ref. [23] with an assumed idler horizontal location of 0.1 m, McMaster–Carr spring (part number 5108N486), and idler radius of 0.01 m. For the method of Ref. [23], the spring was assumed to have no pre-extension.

The initial conditions of our optimization-based approach were $\mathbf{x}_0 = [10, 10]^T$ mm and $\boldsymbol{\beta} = [0.1, 0.1, 0.1, 0.1]^T$. The scalar weights were $w_1 = 10$, $w_2 = w_3 = 0$. No size limit was placed on the cam.

Obviously, the closed-form cam profile 3 shown in Fig. 6(a) is not convex and would pose a problem for design implementation. Our method, on the other hand, remains convex (cam 3). Additionally, as can be seen in Fig. 6(b), the method in Ref. [23] does not respect the extension limits of the spring. Our method, on the other hand, does not violate the extension limits. This more realistic

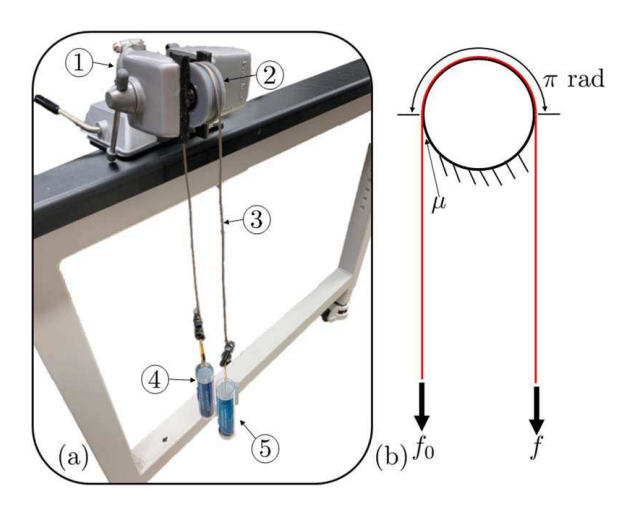


Fig. 5 (a) Friction characterization experimental setup: 1 benchtop vise, 2 cylindrical portion of cam material, 3 wirerope, 4 basket for holding mass that creates f_0 , 5 basket for holding mass that creates f and (b) schematic of experimental setup showing terms used in Eq. (48)

design comes at the cost of 27.87 N mm of root-mean-square error (RMSE) between τ and τ_d .

10.2 Desired Torque Functions. To demonstrate our method, we will solve the optimization problem of Eq. (47) for the following desired torque functions:

$$\tau_{d,1} = m_1 g l_{c_1} \sin(\theta_1) + m_2 g \left[l_1 \sin(\theta_1) + l_{c_2} \sin(\theta_1 + \theta_2) \right]$$

$$\tau_{d,2} = m_2 g l_{c_2} \sin(\theta_1 + \theta_2)$$
(49)

These equations represent the torque required to balance the gravitational load on the joints of the RR manipulator arm shown in Fig. 7. In this equation, m_1 is the mass of link 1; l_{c_1} is the location of the center of mass of link 1; l_1 is the length of link 1; m_2 is the mass of link 2; and l_{c_2} is the center of mass of link 2. The values of the aforementioned link masses and lengths are summarized in Table 1.

We will solve this optimization problem twice: once without trying to minimize the sensitivity of the cam torque to unmodeled changes in the spring constant and once allowing the optimization routine to minimize the aforementioned sensitivity. In the next section, we will discuss the constants and initial conditions used in both simulations.

10.3 Simulation Constants and Initial Conditions. While in some cases, it may be desirable to let the optimization routine select the spring geometries, the springs in this case study were preselected and used as constants. The springs were chosen from McMaster-Carr stock springs. Spring 1 was selected to be part number 5667N212; spring 2 was selected to be part number 7749N634; and spring 3 was selected to be part number 1942N653. The rate and maximum extensions of these springs are shown in Table 2 along with the idler radii, coefficient of friction between the cam and the wire, minimum and maximum cam radii, and the idler vertical offsets. The optimization problems were solved using the active-set algorithm implemented in MATLABTM 2021b's *fmincon* function. The computer used for these simulations is running Windows 10 on an Intel i7-7700 3.6 GHz processor and has 16 GB of RAM. The initial conditions assumed for this simulation were 10 mm of pre-extension for all springs and $\beta_1 = \beta_2 = [0.001, 0.001, 0.001, 0.001]^T$.

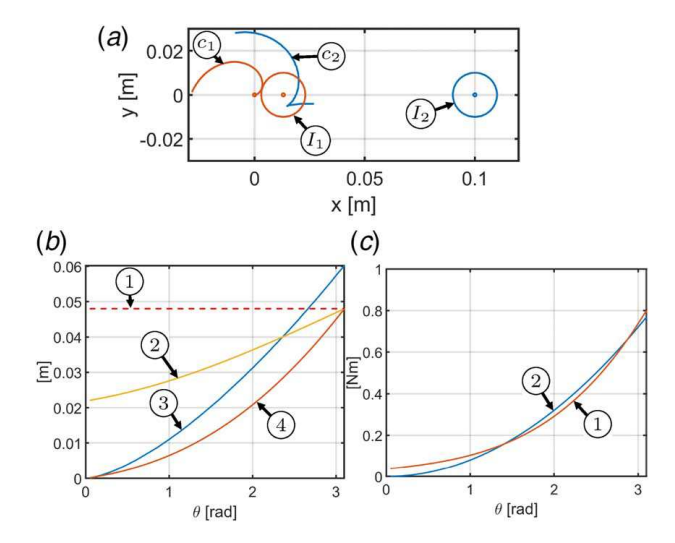


Fig. 6 (a) Cam shapes and idlers for our method (c_1 and I_1) and Ref. [23] (c_2 and I_2) when $\theta=0$, (b) spring deflections: ① maximum allowable spring deflection, ② spring 2 deflection x_2 for our method, ③ spring deflection in Ref. [23], ④ spring 1 deflection x_1 for our method, and (c) desired versus actual torque cam torque for our method: ① our method, ② desired torque

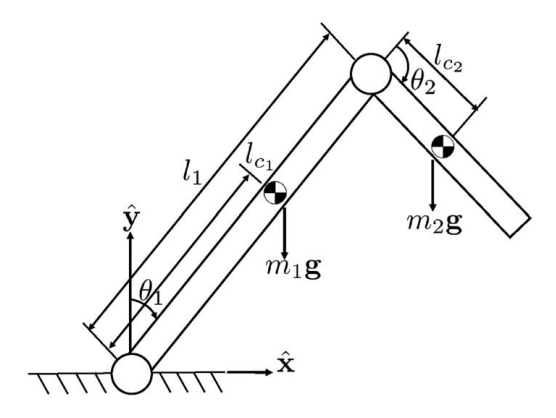


Fig. 7 RR manipulator arm used to generate the desired torque functions

10.4 Two Degrees-of-Freedom System Without Minimizing Sensitivity. For this simulation, the scalar weights were chosen to be $w_1 = w_2 = 10$ and $w_3 = \cdots = w_8 = 0$. Setting w_3 through w_8 to zero makes optimizer not attempt to minimize the sensitivity to changes in spring constant. Figure 8 shows the results of the simulation. Figure 8(a) shows a polar plot of the cam designs; Fig. 8(b) shows the difference between the desired cam 1 torque $\tau_{d,1}$ and the actual cam torque returned by the optimizer τ_1 ; Fig. 8(c) shows the difference between the desired cam 2 torque $\tau_{d,2}$ and the actual cam torque returned by the optimizer τ_2 ; Fig. 8(d) shows the deflection of springs 1 and 3 as a function of θ_1 and θ_2 , respectively. Additionally, the plot shows the maximum allowable deflections in the springs; Fig. 8(e) shows the deflection in spring 2 as a function of θ_1 and θ_2 . It also shows the maximum spring deflection. Table 3 shows the cam polynomial coefficients and spring pre-extensions returned by the optimization routine. Also, Table 3 shows the RMSE and maximum error between τ_1 and $\tau_{d,1}$ and between τ_2 and $\tau_{d,2}$. Our implementation generated these results in 8.60 min.

10.5 Two Degrees-of-Freedom System With Minimizing Sensitivity. For this simulation, the scalar weights were chosen to be $w_1 = w_2 = 1$ and $w_3 = \cdots = w_8 = 1000$. This will cause the optimizer to minimize the sensitivity to changes in spring constant. These values were chosen so that the terms of Eq. (47) have similar magnitudes. Figure 9 shows the results of the simulation. Figure 9(a) shows a polar plot of the cam designs; Fig. 9(b)shows the difference between the desired cam 1 torque $\tau_{d,1}$ and the actual cam torque returned by the optimizer τ_1 ; Fig. 9(c) shows the difference between the desired cam 2 torque $\tau_{d,2}$ and the actual cam torque returned by the optimizer τ_2 ; Fig. 9(d) shows the deflection of springs 1 and 3 as a function of θ_1 and θ_2 , respectively. Additionally, the plot shows the maximum allowable deflections in the springs; Fig. 9(e) shows the deflection in spring 2 as a function of θ_1 and θ_2 . It also shows the maximum spring deflection. Table 4 shows the cam polynomial coefficients and spring pre-extensions returned by the optimization routine. Also, Table 4 shows the RMSE and maximum error between τ_1 and $\tau_{d,1}$ and between τ_2 and $\tau_{d,2}$. Our implementation generated these results in 5.67 min.

10.6 Sensitivity Minimization Results. To demonstrate that the method indeed minimizes the sensitivity of the cam torques,

Table 1 Desired torque function constants

m_1 (kg)	m_2 (kg)	l_{c_1} (m)	l_1 (m)	l_{c_2} (m)	θ
0.5	0.5	0.25	0.5	0.25	[0°, 90°]

Table 2 Simulation constants

$k_1, k_2, k_3 \text{ (N/mm)}$	$x_{1,max}, x_{2,max}, x_{3,max}$ (mm)	$r_1, r_2 \text{ (mm)}$	μ	ρ_{min}, ρ_{max} (mm),	$a_{0_1}, a_{0_2} \text{ (mm)}$
1.10, 7.35, 0.58	57.66, 32.00, 105.00	20, 20	0.3273	25, 500	15, 15

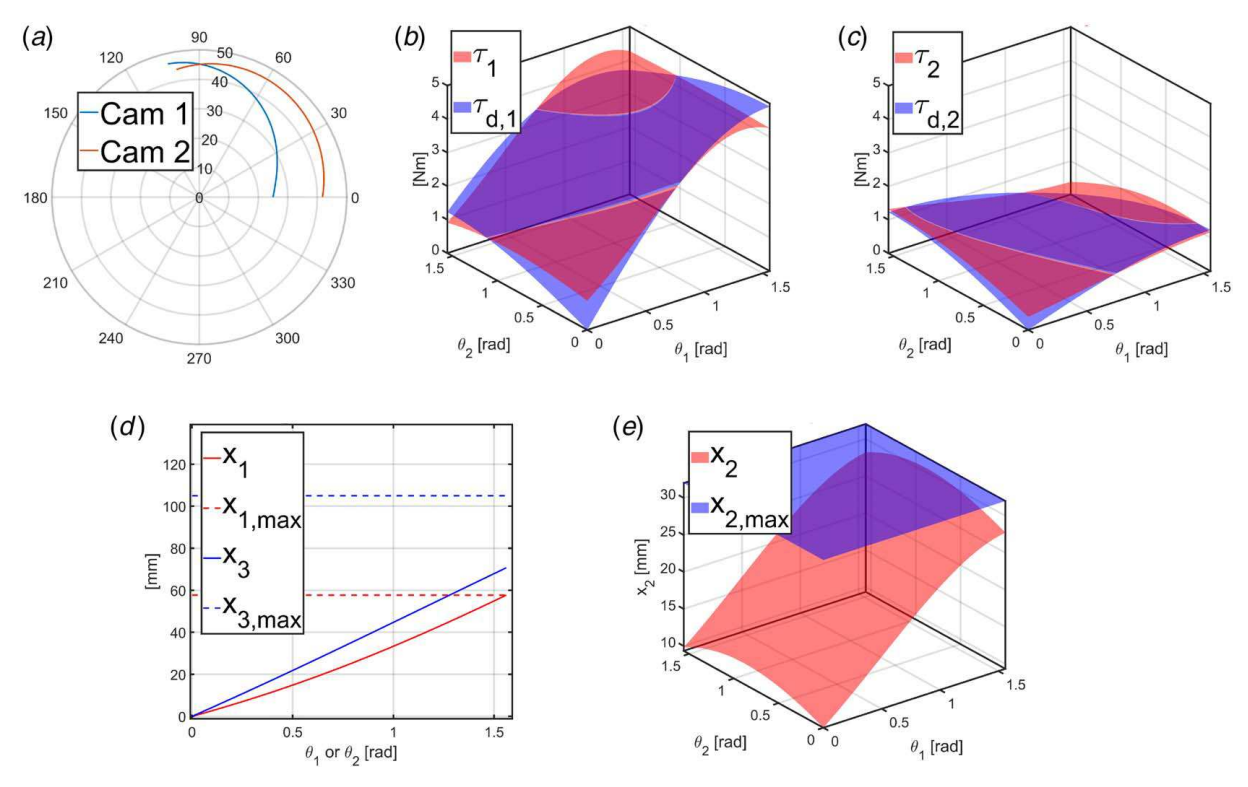


Fig. 8 Two DOF simulation results without sensitivity minimization: (a) cam profiles, (b) τ_1 versus $\tau_{d,1}$, (c) τ_2 versus $\tau_{d,2}$, (d) x_1 , $x_{1,\max}$, x_3 , and $x_{3,\max}$, and (e) x_2 and $x_{2,\max}$

the spring constants shown in Table 2 were increased by 20%, 10%, and 5% and the torque on both cam designs was calculated with the increased spring constants. The RMSEs between the original cam torques and the cam torques with increased spring constants were calculated and the results are shown in Table 5. From these results, it is clear that the deviation in cam torque due to unexpected changes in spring constant is reduced by the optimization routine.

11 Experimental Verification

To experimentally validate our model of the cam torques, we manufactured a desktop prototype of the 2DOF cam system as shown in Fig. 10 using the springs listed in Sec. 10.3. The setup consists of 3D printed cams (Fig. 10① and ②) attached to Hebi™ X8-16 actuators (Fig. 10③). The cams roll against bearing mounted, 3D printed idlers (Fig. 10③) and ④). The idlers are mounted on linear bearings (Fig. 10⑥) between which spring 2 is mounted (Fig. 10⑥). The wire ropes are attached to the cams on one end, pass through grooves in the idlers, and are terminated on springs 1 (Fig. 10⑤) and 3 (Fig. 10⑦).

The torque on the cams is measured using the deflection in the series-elastic elements on the HebiTM actuators. The spring constants of the series-elastic elements were calibrated by applying known moments to the actuators, recording the deflections, and finding the spring constants that best fit the data. The calibrated spring constant for the HebiTM actuator attached to cam 1 was 337.83 Nm/rad and the calibrated spring constant of the Hebi attached to cam 2 was 148.68 Nm/rad.

Table 3 Simulation results without minimizing sensitivity

Parameter	Value		
β_1	$[-0.0052, 0.0133, 0.0046, 0.0250]^{T}$		
β_2	$[-0.0009, -0.0016, 0.0068, 0.0417]^{T}$		
\mathbf{x}_0	[0, 9.33, 0] mm		
τ_1 versus $\tau_{d,1}$ RMSE	243.12 Nmm		
τ_1 versus $\tau_{d,1}$ Max. error	868.25 Nmm		
τ_2 versus $\tau_{d,2}$ RMSE	124.04 Nmm		
τ_1 versus $\tau_{d,2}$ Max. error	389.92 Nmm		

According to the manufacturer, spring 2 has 23.22 N of pretension. However, the spring force given in Eq. (20) assumes there is no pre-tension in the spring. To account for this, the pre-extension in spring 2 given in Table 4 was lowered to 8.52 mm so that the force on the cams from spring 2 when $\theta_1 = \theta_2 = 0$ is equal to the force that was expected using Eq. (20).

As shown in this paper's multimedia extension, ³ both actuators start at $\theta_1 = \theta_2 = 0^\circ$. Cam 1 is kept fixed and cam 2 sweeps from 0° to 90° in 0.02 rad increments. At each increment, 20 torque measurements are taken on each cam. When $\theta_2 = 90^\circ$, θ_1 is incremented by 0.02 rad and then θ_2 decreases to 0° by 0.02 rad increments, taking 20 measurements at each increment. This process is repeated until $\theta_1 = 90^\circ$. The results of this experiment are shown in Fig. 11.

³https://youtu.be/tqnUBkm`f`M

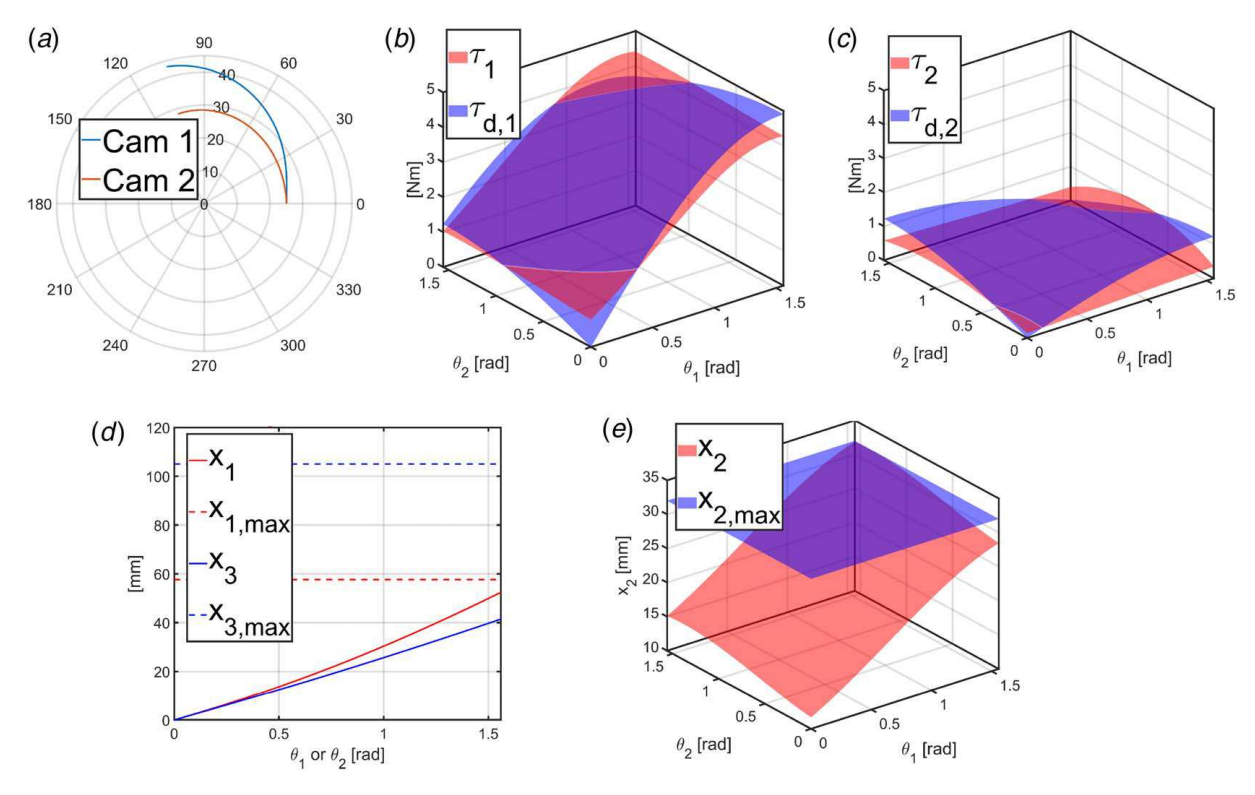


Fig. 9 Two DOF simulation results with sensitivity minimization: (a) cam profiles, (b) τ_1 versus $\tau_{d,1}$, (c) τ_2 versus $\tau_{d,2}$, (d) x_1 , $x_{1,\max}$, x_3 , and $x_{3,\max}$, and (e) x_2 and $x_{2,\max}$

Table 4 Simulation results with minimizing sensitivity

Parameter	Value		
β_1	$[-0.0041, 0.0125, 0.0007, 0.0250]^{T}$		
β_2	$[-0.0019, 0.0052, -0.0014, 0.0251]^{T}$		
\mathbf{x}_0	$[0, 11.68, 0]^{\mathrm{T}}$ mm		
τ_1 versus $\tau_{d,1}$ RMSE	415.00 Nmm		
τ_1 versus $\tau_{d,1}$ Max. error	788.33 Nmm		
τ_2 versus $\tau_{d,2}$ RMSE	384.84 Nmm		
τ_2 versus $\tau_{d,2}$ Max. error	428.17 Nmm		

In this test, the RMSE between the model predicted torque and the actual torque for cam 1 was 353.0 Nmm. However, when friction was ignored, the RMSE increased to 518.6 Nmm. The RMSE between the model predicted torque and the actual torque for cam 2 was 166.3 Nmm. With infinite friction, the RMSE was 174.1 Nmm. The RMSE between the actual torque and $\tau_{d,1}$ was 579.9 Nmm and 356.2 Nmm between the actual torque and $\tau_{d,2}$.

Potential sources of error in this experiment include the accuracy and noise of the torque sensing on the Hebi actuators, friction in the linear bearings, the accuracy of the friction characterization experiment from Sec. 9, inexact pre-extension adjustment, and deflection/hysteresis in the wire rope. Additionally, the stiffness of springs 1–3

were assumed to be equal to the manufacturer-specified value. This assumption introduced additional error between the experimental and model predicted torques.

12 Discussion

While this method is guaranteed to return a physically realizable cam system, there is no guarantee that the resulting cam torques will exactly match the desired torque. We believe this is acceptable for robotic applications where the actuators are able to compensate for differences between the static torques and the torques provided by the cams. For discontinuous or highly non-monotonic desired torque profiles, the torque matching performance will degrade. Additionally, if the desired torque on one of the cams is a stronger function of the other cam angle than of its own angle, the optimization routine may struggle to match the desired torque profile. However, some of this can be alleviated by increasing $|a_0|$ (i.e., increasing the moment arm of spring 2's force). Additionally, if the constraints on the cam design (e.g., ρ_{min} , $\sim \rho_{max}$, etc.) are too narrow, the desired and actual torques may not match well. Additionally, this cam design only works for scenarios when the distance between the cam centers of rotation remains constant.

Because the partial derivative of the cam torques with respect to the spring constants (Eqs. (43) and (44)) are strong functions of the

Table 5 Deviation in cam torque after increase in spring constants

		Without Sens. Min. (Fig. 8)	With Sens. Min. (Fig. 9)	Reduction in RMSE
20% increase	Cam 1 RMSE	702.76 Nmm	647.05 Nmm	55.71 Nmm
	Cam 2 RMSE	204.69 Nmm	143.84 Nmm	60.85 Nmm
10% increase	Cam 1 RMSE	351.38 Nmm	323.52 Nmm	27.86 Nmm
	Cam 2 RMSE	102.34 Nmm	71.92 Nmm	30.42 Nmm
5% increase	Cam 1 RMSE	175.69 Nmm	161.76 Nmm	13.93 Nmm
	Cam 2 RMSE	51.17 Nmm	35.961 Nmm	15.21 Nmm

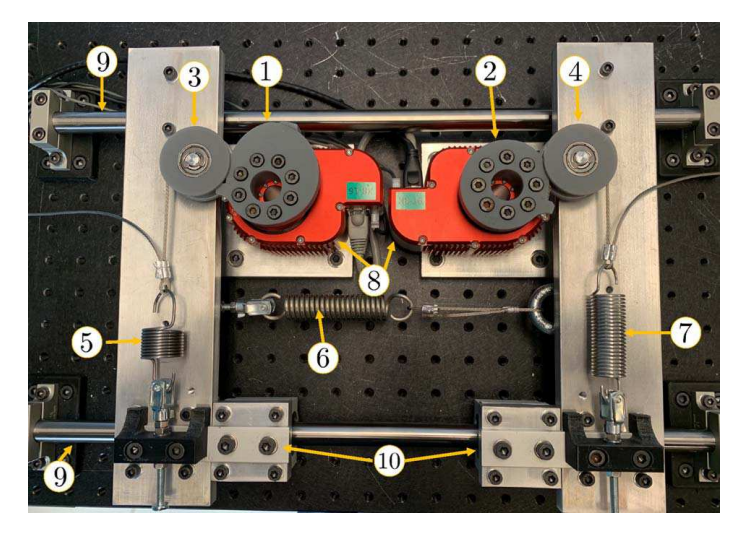


Fig. 10 Experimental setup: 0 cam 1, 0 cam 2, 3 idler 1, 0 idler 2, 3 spring 1, 0 spring 2, 0 spring 3, 0 HebiTM X8-16 actuator, 0 linear shaft, and 0 linear ball bearing

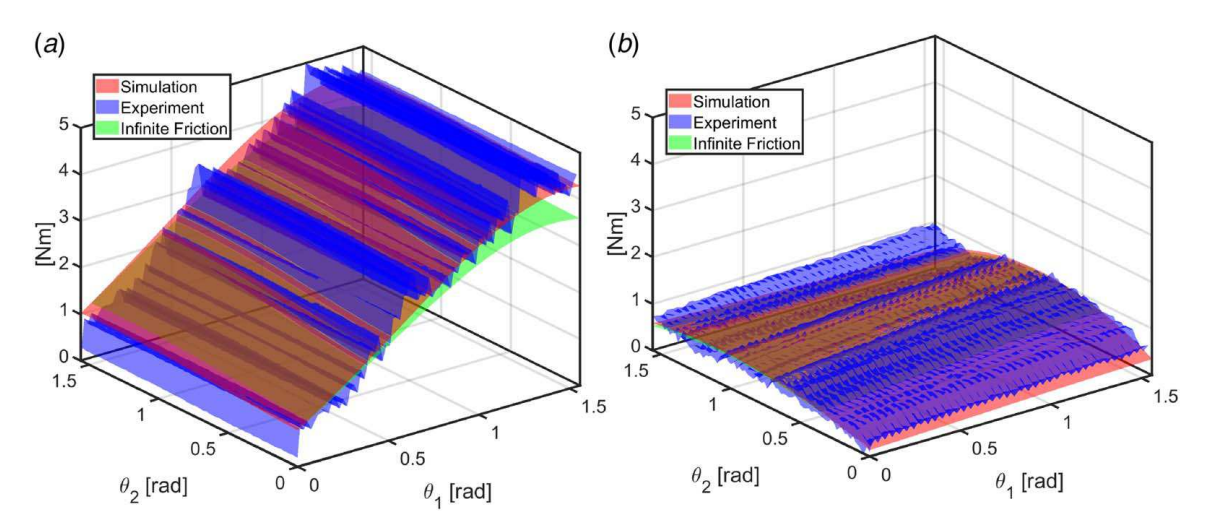


Fig. 11 Experimental cam torques compared to simulated cam torques with friction model and simulated cam torques with infinite friction: (a) cam 1 and (b) cam 2

spring deflections and cam-idler contact point locations, minimizing the sensitivity to unexpected changes in spring constant is essentially equivalent to minimizing the size of the cams. This means that increasing values of w_3 through w_8 will sometimes decrease how well the torque matches the desired torque.

Lastly, the friction model presented in Sec. 4.1 has less impact on the torque for relatively circular cams. This is because the distributed forces that are locally perpendicular to the cam \mathbf{f}_c pass through the cam center of rotation and therefore cannot create a moment about the cam center of rotation. This can be seen in the experimental results presented in Sec. 11. In Fig. 11(a), the difference between the finite and infinite torque curves is much larger than in Fig. 11(b). This is because cam 2 is much closer to circular than cam 1, which can be seen in Figs. 9(a) and 10.

13 Conclusions

Collaborative robots must simultaneously pose minimal risk to workers and be powerful enough to assist workers in industrial tasks such as lifting heavy equipment. One method for navigating these conflicting design requirements is through the use of static balancing mechanisms to offset the robot's self-weight, thus enabling the selection of low-powered (i.e., safer) actuators.

Because of their simple, lightweight, and compact design, wire-wrapped cam mechanisms are a promising option for static balancing. However, previous works on wire-wrapped cam mechanisms can return non-convex cams, require unrealistically long spring torques, and ignore the effect of friction between the wire and the cam. These methods are also sensitive to unmodeled deviations in spring constant.

To address these limitations, in this paper, we presented the design of a novel, two DOF wire-wrapped cam system where the torque on each cam is a function of both cam angles. We also presented a model of how the friction and distributed pressure between the cam and the wire affects the torque on the cams. This friction model takes into account the distributed friction and contact pressure between the wire and the cam. This relaxes key assumptions made in previous works that treated the torque on the cam as resulting from a single point force at the wire tangency point. Using this model, we presented an optimization-based cam design procedure that (1) ensured the cam is convex, (2) guaranteed the spring deflections stay below the maximum allowable values, and (3) minimized sensitivity to unexpected changes in spring constant.

Using this cam design method, we built a prototype of the proposed mechanism and experimentally determined that our model predicts the torque on the cams to within 353.0 Nmm of root mean square error. The results also indicate that the distributed

force between the wire and the cam can have a significant effect on cam torque for more non-circular cams.

Acknowledgment

This work was supported by NSF award #1734461 and by Vanderbilt internal university funds. A. Orekhov was partially supported by the NSF Graduate Research Fellowship under #DGE-1445197.

Conflict of Interest

There are no conflicts of interest.

Data Availability Statement

No data, models, or code were generated or used for this paper.

References

- [1] U.S. Bureau of Labor Statistics, 2016, Nonfatal Occupational Injuries and Illnesses Requiring Days Away From Work, 2015. [online.] Available https:// www.bls.gov/news.release/pdf/osh2.pdf.
- [2] Hales, T., and Bernard, B., 1996, "Epidemiology of Work-Related Musculoskeletal Disorders," Orthop. Clin. N. Am., 27(4), pp. 679–709.
- [3] Vermeulen, M., and Wisse, M., 2010, "Intrinsically Safe Robot Arm: Adjustable Static Balancing and Low Power Actuation," Int. J. Soc. Rob., 2(3), pp. 275-288.
- [4] Laliberte, T., Gosselin, C., and Jean, M., 1999, "Static Balancing of 3-DOF Planar Parallel Mechanisms," IEEE/ASME Trans. Mechatron., 4(4), pp. 363–377.
- [5] Whitney, J. P., and Hodgins, J. K., 2014, "A Passively Safe and Gravity-Counterbalanced Anthropomorphic Robot Arm," Proc. IEEE Int. Conf. Rob. Autom., 6168(3), pp. 6168-6173.
- [6] Petrescu, R. V., Aversa, R., Apicella, A., and Petrescu, F. I. T., 2018, "Total Static Balancing and Kinetostatics of the 3R Base Cinematic Chain," J. Mechatron. Rob., **2**(1), pp. 1–13.
- [7] Woo, J., Seo, J.-T., and Yi, B.-J., 2019, "A Static Balancing Method for Variable Payloads by Combination of a Counterweight and Spring and Its Application as a Surgical Platform," Appl. Sci., 9(19), p. 3955.
- [8] Gopalswamy, A., Gupta, P., and Vidyasagar, M., 1992, "A New Parallelogram Linkage Configuration for Gravity Compensation Using Torsional Springs, Proceedings of 1992 IEEE International Conference on Robotics and Automation, Nice, France, May 12-14, Vol. 1, IEEE Computer Society Press,
- [9] Agrawal, A., and Agrawal, S. K., 2005, "Design of Gravity Balancing Leg Orthosis Using Non-Zero Free Length Springs," Mech. Mach. Theory, 40(6), pp. 693-709.
- [10] Barents, R., Schenk, M., van Dorsser, W. D., Wisse, B. M., and Herder, J. L., 2011, "Spring-to-Spring Balancing as Energy-Free Adjustment Method in Gravity Equilibrators," ASME J. Mech. Des., 133(6), p. 061010.
- [11] Kim, H.-S., and Song, J.-B., 2013, "Low-Cost Robot Arm With 3-DOF Counterbalance Mechanism," 2013 IEEE International Conference on Robotics and Automation, Karlsruhe, Germany, May 6-10, IEEE, pp. 4183-4188.
- [12] Ahn, K. H., Lee, W. B., and Song, J. B., 2016, "Reduction in Gravitational Torques of an Industrial Robot Equipped With 2 DOF Passive Counterbalance Mechanisms," IEEE International Conference on Intelligent Robots and Systems, Daejeon, South Korea, Oct. 9-14, pp. 4344-4349.
- [13] Chu, Y. L., and Kuo, C. H., 2016, "A Single-DOF Self-Regulated Gravity Balancer for Adjustable Payload," Proceedings of the ASME Design Engineering Technical Conference, Charlotte, NC, Aug. 21-24, 5A-2016.
- [14] Takahashi, T., Zehnder, J., Okuno, H. G., Sugano, S., Coros, S., and Thomaszewski, B., 2019, "Computational Design of Statically Balanced Planar Spring Mechanisms," IEEE Rob. Autom. Lett., 4(4), pp. 4438–4444.
 [15] Simionescu, I., 2000, "The Static Balancing of the Industrial Robot Arms Part II:
- Continuous Balancing," Mech. Mach. Theory, 35(9), pp. 1299–1311. [16] Wu, C. J., and Angeles, J., 2001, "Optimum Synthesis of an Elastic Torque-Compensating Cam Mechanism," Mech. Mach. Theory, 36(2), pp. 245–259.
- [17] Koser, K., 2009, "A Cam Mechanism for Gravity-Balancing," Mech. Res. Commun., 36(4), pp. 523–530.
- [18] Lee, G., Lee, D., and Oh, Y., 2018, "One-Piece Gravity Compensation Mechanism Using Cam Mechanism and Compression Spring," Int. J. Precis. Eng. Manuf. Green Technol., 5(3), pp. 415-420.
- [19] Buśkiewicz, J., 2019, "Balancing of a Wire Rope Hoist Using a Cam Mechanism," Advances in Manufacturing II, B. Gapiński, M. Szostak, and V. Ivanov, eds., Springer International Publishing, Poznan, Poland, pp. 25-35.

- [20] Harrington, R., 1951, "Generation of Functions by Windup Mechanisms," Rev. Sci. Instrum., 22(9), pp. 701-702.
- [21] Carlson, L. E., and Childress, D., 1975, "The Lift Lock: A Device to Increase the Lifting Ability of Dual-Control Prostheses," Bull. Prosthet. Res., 10(23), pp. 158-
- [22] Tidwell, P. H., Bandukwala, N., Dhande, S. G., Reinholtz, C. F., and Webb, G., 1994, "Synthesis of Wrapping Cams," ASME J. Mech. Des., 116(2), pp. 634-638
- [23] Kilic, M., Yazicioglu, Y., and Kurtulus, D. F., 2012, "Synthesis of a Torsional Spring Mechanism With Mechanically Adjustable Stiffness Using Wrapping Cams," Mech. Mach. Theory, 57, pp. 27-39.
- [24] Schroeder, J. S., and Perry, J. C., 2017, "Development of a Series Wrapping Cam Mechanism for Energy Transfer in Wearable Arm Support Applications," IEEE International Conference on Rehabilitation Robotics, London, UK, July 17-20, pp. 585-590.
- [25] Spagnuolo, G., Malosio, M., Dinon, T., Molinari Tosatti, L., and Legnani, G., 2017, "Analysis and Synthesis of Linwwc-vsa, a Variable Stiffness Actuator for Linear Motion," Mech. Mach. Theory, 110, pp. 85-99.
- [26] Schroeder, J. S., and Perry, J. C., 2018, "Development of a Series Wrapping Cam and Energy-Storing Spring System for Application in Wearable Robotic Arm Supports," Technol. Innov., 20(1-2), pp. 21-36.
- Yigit, C. B., Bayraktar, E., and Boyraz, P., 2018, "Low-Cost Variable Stiffness Joint Design Using Translational Variable Radius Pulleys," Mech. Mach. Theory, 130(111), pp. 203-219.
- [28] Fedorov, D., and Birglen, L., 2018, "Differential Noncircular Pulleys for Cable Robots and Static Balancing," ASME J. Mech. Rob., 10(6), p. 061001.
- [29] Kim, D.-W., Lee, W.-B., and Song, J.-B., 2020, "Design of a Linear Gravity Compensator for a Prismatic Joint," IEEE/RSJ International Conference on Intelligent Robots and Systems (IROS), Las Vegas, NV, Oct. 24, 2020-Jan. 24, 2021, pp. 6440-6445.
- [30] Candan, S. C., Karagöz, O. K., Yazıcıoğlu, Y., and Saranl, U., 2020, "Design of a Parallel Elastic Hopper With a Wrapping Cam Mechanism and Template Based Virtually Tunable Damping Control," Proceedings of the ASME 2020 Dynamic Systems and Control Conference. Volume 1: Adaptive/Intelligent System Control, Virtual, Oct. 5-7, American Society of Mechanical Engineers, p. V001T05A009.
- [31] Qu, X., Cao, D., Qu, R., Zhang, G., and Zhang, S., 2022, "A Novel Design of Torsion Spring-Connected Non-Linear Stiffness Actuator Based on Cam Mechanism," ASME J. Mech. Des., 144(8), p. 083303.
- Simionescu, I., 2000, "The Static Balancing of the Industrial Robot Arms Part I: Discrete Balancing," Mech. Mach. Theory, 35(9), pp. 1287–1298.
- [33] Morita, T., Kuribara, F., Shiozawa, Y., and Sugano, S., 2003, "A Novel Mechanism Design for Gravity Compensation in Three Dimensional Space," Proceedings 2003 IEEE/ASME International Conference on Advanced Intelligent Mechatronics (AIM 2003), Kobe, Japan, July 20-24, IEEE, Vol. 1, pp. 163-168.
- [34] Lee, W.-B., Lee, S.-D., and Song, J.-B., 2017, "Design of a 6-DOF Collaborative Robot Arm With Counterbalance Mechanisms," 2017 IEEE International Conference on Robotics and Automation (ICRA), Singapore, May 29-June 3, pp. 3696-3701.
- [35] Cho, C., Lee, W., and Kang, S., 2010, "Static Balancing of a Manipulator With Hemispherical Work Space," 2010 IEEE/ASME International Conference on Advanced Intelligent Mechatronics, Montreal, QC, Canada, July 6-9, IEEE, pp. 1269-1274.
- [36] Cho, C., Lee, W., Lee, J., and Kang, S., 2012, "A 2-DOF Gravity Compensator With Bevel Gears," J. Mech. Sci. Technol., 26(9), pp. 2913–2919
- [37] Mahalingam, S., and Sharan, A., 1986, "The Optimal Balancing of the Robotic Manipulators," Proceedings of 1986 IEEE International Conference on Robotics and Automation, San Francisco, CA, Apr. 7-10, Vol. 3, pp. 828-835.
- [38] Lessard, S., Bigras, P., and Bonev, I. A., 2007, "A New Medical Parallel Robot and Its Static Balancing Optimization," ASME J. Med. Devices, 1(4), pp. 272-
- [39] Demeulenaere, B., and De Schutter, J., 2005, "Input Torque Balancing Using an Inverted Cam Mechanism," ASME J. Mech. Des., 127(5), pp. 887-900.
- [40] Saravanan, R., Ramabalan, S., and Dinesh Babu, P., 2008, "Optimum Static Balancing of an Industrial Robot Mechanism," Eng. Appl. Artif. Intell., 21(6), pp. 824-834.
- [41] Moré, J. J., 1978, "The Levenberg-Marquardt Algorithm: Implementation and Theory," Numerical Analysis, G. A. Watson, ed., Springer, Berlin, Heidelberg, pp. 105-116.
- [42] Antman, S. S., 2004, Nonlinear Problems of Elasticity, 2nd ed., Springer, New York
- [43] Meriam, J. L., and Kraige, L. G., 2012, Engineering Mechanics: Statics, 7th ed., John Wiley & Sons, Hoboken, NJ. [44] Angeles, J., and López-Cajún, C. S., 2012, Optimization of Cam Mechanisms,
- Vol. 9. Kluwer Academic Publishers, Dordrecht, The Netherlands, [45] Bajaj, C., and Kim, M. S., 1991, "Convex Hulls of Objects Bounded by Algebraic
- Curves," Algorithmica, 6(1), p. 533.
- [46] Belegundu, A. D., and Zhang, S., 1992, "Robustness of Design Through Minimum Sensitivity," ASME J. Mech. Des., 114(2), pp. 213-217.